

https://dspace.org/

Mossbauer effect studies at low temperatures

Hearne, Giovanni Rosano

2015-01-26
http://hdl.handle.net/10539/16750

Downloaded from a DSpace repository. https://dspace.org/

MÖSSBAUER EFFECT STUDIES AT LOW TEMPERATURES

Giovanni Rosano Hoarne

A Research Project Submitted To The Faculty Of Science,
University Of The Witwatersrand, Johannesburg
In Partial Fulfillment Of The Requirements For The
Degree Of Master of Science.

Johannesburg 1985

DECLARATION

I declare that this research project is my own, unaided work. It is being submitted in partial fulfillment of the requirements for the degree of Master of Science at the University of the Witwatersrand, Johannesburg. It has not been submitted before for any degree or examination in any other University.

Giovanni Rosano Hearne

16th day of September, 1985.

ABSTRACT

A facility has been built to enable Mössbauer-effect spectroscopy at low temperatures. The temperature of the sample can be varied from as low as 1.5 K to room temperature. With this facility studies were performed on superconducting tin compounds using the ^{119}Sn Mössbauer isotope. Sn atoms are non-magnetic and, instead of acting as a poisoner of superconductivity, they provide sites at which investigations on an atomic scale can be carried out. Presented here are the results of studies on a sample of commercial superconducting Nb-Sn tape, used for important technological applications such as windings in superconducting magnets. In the preparation of the tape, various Nb-Sn phases are formed of which β-Nb_3Sn is the desired phase because it has a high superconducting transition temperature, T_c = 18 K. The other phases have superconducting temperatures below 4 K. Mössbauer spectra were recorded in the range 300 K to 4.2 K. The room temperature spectra allowed the identification of the Nb-Sn phases present. The results reveal that the sample contained 40% Nb_3Sn, 16% $NbSn_2$ and 44% β-Sn. In addition to the phase analysis, the mean-square displacement of Sn in the various phases as a function of temperature was determined from the temperature evolution of the Mössbauer spectra. In the case of the high T_c Nb_3Sn phase, the mean-square displacement of Sn as a function of temperature shows remarkably different behavior from that of the low T_c phases $NbSn_2$ and β-Sn. This indicates a possible correlation between T_c and the lattice behavior of a superconducting compound.

TABLE OF CONTENTS

LIST OF FIGURES 2

LIST OF TABLES 6

1. INTRODUCTION 7

2. THE MÖSSBAUER EFFECT 12

3. THE MÖSSBAUER SPECTROMETER 22

4. THE LOW TEMPERATURE APPARATUS 30

5. MÖSSBAUER EFFECT STUDIES ON NB-SN COMPOUNDS 39

ACKNOWLEDGEMENTS 58

REFERENCES 59

LIST OF FIGURES

		Page
Fig. 1.1.1	Temperatures at which some selected phenomena occur. Note the logarithmic scale.	8
Fig. 2.2.1	(a) The γ-ray resulting from nuclear decay in a free nucleus and the corresponding nuclear absorption by an identical nucleus. E_o must match E_o' to within 10^{-8} eV for the process to occur. (b) A schematic of the setup used to measure nuclear absorption of γ-rays.	13
Fig. 2.3.1	(Top) The allowed nuclear transitions when the excited state and ground state is split due to the magnetic hyperfine field. (Bottom) Note the decrease in transmission at each of the allowed nuclear transitions in the absorber as reflected in the ME spectrum obtained using ^{57}Fe Mössbauer nuclei, with iron foil as the absorber and ^{57}Co in rhodium as the source.	16
Fig. 2.4.1	Quadrupole splitting for a spin 3/2 → 1/2 transition.	18
Fig. 3.1.1	An overview of the low-temperature ME facility for use in the transmission geometry.	23

		Page
Fig. 3.2.1	(a) A photograph of pulses resulting from radiative transitions in a $CaSnO_3$ source as they appear at the output of an amplifier. (b) The ADC process.	25
Fig. 3.5.1	Velocity calibration system.	29
Fig. 3.5.2	A velocity calibration spectrum. The counts in each channel represent the velocity associated with that channel.	29
Fig. 4.1.1	A schematic diagram of the Janis Mössbauer cryostat.	31
Fig. 4.1.2	The experimental setup as viewed from (a) above, (b) the side.	33
Fig. 4.1.3	The gas distribution facility and pumping system used for He recovery and used to achieve temperatures as low as 1.5 K.	34
Fig. 4.1.4	He consumption in the cryostat.	35
Fig. 4.2.1	Calibration curves of the resistors used for temperature control and measurement.	37
Fig. 4.2.2	A block diagram of the temperature regulator.	38
Fig. 5.1.1	The phase diagram of the Nb-Sn system. (Figure taken from Charlesworth et al. 1970.)	40
Fig. 5.2.1	The nuclear decay scheme of the ^{119m}Sn Mössbauer isotope.	42
Fig. 5.2.2	A proportional counter pulse height spectrum of the source.	43

		Page
Fig. 5.2.3	(a) An Aptec Ge detector pulse height spectrum of the source showing most of the radiative transitions; a palladium filter was used. (b) A pulse height spectrum showing only the more important transitions. Compare this spectrum with that of fig. 5.2.2.	44
Fig. 5.5.1	(a) A calibration spectrum indicating the velocity as a function of channel (solid line). The dash-dot-dash line represents the base line B relative to the base line value N_o obtained when the source is stationary. (b) A spectrum and its mirror image resulting from the drive motion in (a).	47
FIG. 5.6.1	Mössbauer spectrum of Nb-Sn superconducting tape at room temperature.	49
Fig. 5.6.2	Temperature evolution of the Mossbauer spectrum. Additional spectra measured at 87 K, 13 K and 9 K, are not shown.	51
Fig. 5.6.3	A plot of $ln(A_1/A_2)$ versus temperature, where A_2 is the absorption area of the β-Sn component and A_1 is the absorption area of the Nb_3Sn component (a) ; (b) refers to the $NbSn_2$ component.	52
Fig. 5.7.1	(a) Pair potential ϕ. (b) The atomic potential ϕ_a when the interatomic spacing a is about r_o ; h is in reasonable approximation parabolic. (c) ϕ_a deviates from parabolic behavior when the interatomic spacing is larger than r_o.	54

		Page
Fig. 5.7.2	The msd of an atom in the harmonic approximation (a); (b) in a potential as shown in fig. 5.7.1 (b); (c) in a highly anharmonic potential as shown in fig. 5.7.1 (c), according to Dash et al. (1968).	55
Fig. 5.7.3	The msd as a function of temperature for the various Nb-Sn phases present relative to the β-Sn measurements of Hohenemser (1965). The dotted lines represent harmonic behavior. The solid lines are drawn to guide the eye.	56

LIST OF TABLES

		Page
Table 5.1.1	The crystal structure and superconducting transition temperature of various Nb-Sn compounds (from the CRC Handbook of Chemistry and Physics, 60th edition).	40
Table 5.6.1	Parameters (in mm/s) for a room temperature spectrum as obtained with MÖSSFUN in a least squares fit of the data (χ^2 = 1.04) compared with values obtained in other measurements (Sitek et al. 1978, Mössbauer Effect Data Index -- Covering the 1970 Literature, p. 23).	50

1. INTRODUCTION

1.1 Significance of low temperatures.

Currently available technology enables the cooling of copper nuclei to 5×10^{-8} K and the heating of a plasma in a tokamak to 10^8 K (*fig. 1.1.1*). It is not surprising that the properties of materials undergo considerable modifications in this huge range. Many of these changes are of profound significance not only for basic physics, but also for practical applications. It is of interest to point out that the changes in properties of a material often seem to be related more to the factor by which the absolute temperature is varied than to the magnitude of the variation. Thus a change by a factor ten in going from 15 K to 1.5 K -- a temperature range of only ... K -- brings about, on the average, as large a change in properties as would result from a temperature change of a factor ten in going from 1500 K to 150 K -- a temperature range of 1350 K.

In the range from 300 K to 3 K the temperature varies by two orders of magnitude and substantial changes in the properties of a solid can be expected. An example is the onset of superconductivity at some low temperature T_c ($\leq$ 23 K), a phenomenon for which no known analogue exists at room temperature.

1.2 An effective microprobe -- the Mössbauer Effect.

The foregoing comments stress the significance of research at low temperatures and lead to the question, what is an effective way of probing the material of interest ?

Rudolf L. Mössbauer realized in 1958 that the nucleus of an atom bound in a solid may not recoil when it emits or absorbs a γ-ray. The probability for the occurrence of such a process is called the recoilless fraction f. In a recoilless process the entire energy of the nuclear transition is transferred to the γ-ray which then has the proper energy to excite a nucleus in an absorber. The phenomenon of recoilless emission of γ-rays and their absorption by identical

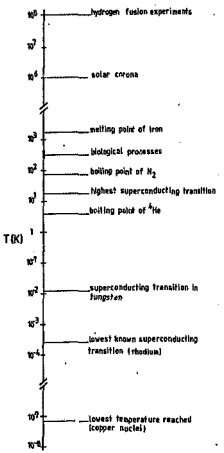


Fig. 1.1.1 Temperatures at which some selected phenomena occur. Note the *logarithmic scale*.

nuclei constitute the essential elements of the Mössbauer effect (ME), a discovery which was recognized by the award of the Nobel Prize in 1961.

The most important aspect of the Mössbauer effect resides not in the discovery of the recoil-free processes themselves but in the fact that these processes make available γ-rays with an energy which is very sharply defined. Typically, the uncertainty Γ_0 in the γ-ray energy is of the order of 10^{-8} eV while the

energy of the recoilless γ-ray is of the order of 10 keV. This resolution of 1 part in 10^{12} makes it possible to measure accurately various interactions of the nuclear moments with their environment. These interactions, called the hyperfine (hf) interactions, cause changes in the nuclear transition energies which are usually larger than Γ_o thus permitting their precise measurement. This makes it possible to study the effective magnetic field or the electric field gradient at the nucleus which depend both on the electric configuration of the atom and on the symmetry of the distribution of the neighboring charges.

Another important application is based on the isomer shift which measures the electrostatic interaction of the nucleus with the extranuclear electrons at the nuclear site; it gives information on the covalence of chemical binding and electronic structure in general.

Information on the lattice dynamics of a solid can be obtained from the recoilless fraction. The recoilless fraction as a function of temperature gives us a picture of how the phonon spectrum changes with temperature.

1.3 Superconductivity.

In the low temperature regime, some solids show zero resistance below a well-defined critical temperature T_c. This phenomenon is called superconductivity. It is found in a wide variety of materials : metallic elements, alloys, intermetallic compounds and, recently, synthetic organic solids, which in the normal state are poor conductors.

Superconductors can be divided into two types, depending on their behavior in an applied magnetic field. The distinction is made on the basis of how flux penetrates into the bulk of a material. In an ideal situation, the flux does not penetrate into a type I superconductor until a critical field H_c is reached, and then it does so discontinuously. By contrast, in a type II superconductor, the flux does not penetrate until a lower critical field H_{c1} : partial flux penetration can then occur over a wide range of applied field values, even though the zero resistance property may be maintained up to a limiting applied field, called the upper critical field H_{c2}, of more than 20 T in some materials. This property is

of particular importance in the technological exploitation of superconductors for high-current and high-field applications.

The microscopic description of the superconducting state is contained in the (BCS) theory of Bardeen, Cooper and Schreiffer (1957). The fundamental postulate of this theory is that superconductivity occurs when an attractive interaction between two electrons, by means of phonon exchange, dominates the *repulsive screened* Coulomb interaction. In the superconducting state the conduction electrons form bound pairs called *Cooper pairs*. The existence of an attractive interaction between pairs of electrons arises from the distortion of the lattice. This distortion propagates through the lattice via phonons and affects a second electron some distance away. The interaction between the two electrons through propagating lattice distortions is attractive and thus in the superconducting state, the lattice plays an important role.

Superconductivity is well described by the phenomenological Ginzburg-Landau theory and the microscopic BCS theory. However these theories are *unable to predict a priori* superconducting materials or transition temperatures. Empirical rules have been established (Matthias 1957) which provide this information. For example, in all cases involving transition metals, the variation of T_c shows sharp maxima for the number of valence electrons per atom equal to three, five and seven. However, recently discovered ternary compounds involving transition metals violate this rule (Matthias 1976, p. 635).

From considerations of the microscopic picture of superconductivity, there ought to exist correlations between T_c and the lattice dynamical properties and electronic structure of a solid. Information on the lattice dynamics and the electronic structure can be obtained through Mössbauer studies. Furthermore, the ME does not involve the application of magnetic fields during measurements in contrast to other techniques (bulk susceptibility measurements), so the superconducting state is not perturbed.

The ^{119}Sn isotope ranks second in importance to that of ^{57}Fe in ME spectroscopy. The tin atom does not carry an intrinsic spin moment in any of its compounds. This non-magnetic property makes the tin isotope favorable for the microprobing of superconductors on whose properties magnetic fields have a

debilitating effect. ^{119}Sn Mössbauer spectroscopy has previously been used to study superconductors. Earlier, experimenters found anomalous behavior of the f value in Sn at temperatures close to the superconducting transition temperature. However, the careful f value measurements of Hohenemser (1965) did not reveal *any anomalies*. Another interesting system $V_3Ga_xSn_{1-x}$ has been studied by Kimball et al. (1974). This system has a high superconducting transition temperature ($T_c \sim 15$ K) for low concentrations of Sn. ^{119}Sn ME studies have also been performed on the technologically important high T_c superconductor Nb_3Sn (see §5.1).

Superconducting materials merit investigation because our understanding of the fundamental physical laws that govern their behavior is incomplete and because of their importance in technological applications. The foregoing comments indicate that the ME is an ideal tool for probing these materials.

1.4 Outline of research.

In this research project a low temperature facility has been set up to allow Mössbauer-effect studies on superconducting compounds. Chapter 2 outlines principles of the ME, the hyperfine interactions and lattice dynamics. A description of the ME spectrometer and low temperature apparatus is presented in chapter 3 and chapter 4, respectively. Finally, chapter 5 describes ^{119}Sn Mössbauer-effect studies on superconducting Nb-Sn compounds.

2. THE MÖSSBAUER EFFECT

2.1 Introduction.

The γ-ray resulting from a nuclear transition will be absorbed by an identical nucleus if its energy matches the transition energy E_o to within about 10^{-8} eV (see *fig. 2.1.1 (a)*). The law of conservation of momentum requires that, in the rest frame of the nucleus, the nucleus must recoil with a momentum equal to that carried away by the γ-ray. This means that a nucleus of mass M is given a recoil energy $E_R = \hbar^2k^2/2M$ where k is the γ ray wave vector. The energy of the γ-ray will then not be E_o but $E_o - E_R$. Similarly, if a γ-ray is absorbed by exciting a nucleus in the ground state, it must have an energy $E_o + E_R$. Thus the effect of recoil means that the γ-ray will have an energy deficit of $2E_R$ for nuclear excitation. In a typical γ-ray emission process E_R is of the order of 10^{-3} to 10^{-2} eV so that the effect of recoil is sufficient to cause a mismatch of the γ-ray energy and the excitation energy required for nuclear absorption. However, Mössbauer discovered that when nuclei are embedded in a solid a certain number of the γ-rays are emitted and absorbed without exciting lattice vibrations. In that case the entire lattice shares the recoil E_R which is inversely proportional to the mass of the recoiling object, that is, the γ-ray will experience negligible recoil energy loss and is then able to excite a nucleus in the absorber. The recoilless emission and absorption of γ-rays is known as the Mössbauer effect.

Recoillessly emitted γ-rays have a Lorentzian energy distribution with full-width at half maximum $\Gamma_o = \hbar/\tau$, where τ is the half-life of the excited state. The absorption cross section for recoilless absorption is given by a similar function. The energy of an emitted γ-ray can be varied by imparting to it a velocity v. Nuclear absorption in an identical nucleus will occur at the velocity v_o corresponding to the transition energy E_o. The measurement of the transmitted intensity of the γ-rays through an absorber as a function of the velocity v of the source relative to the absorber constitutes the usual Mössbauer experiment

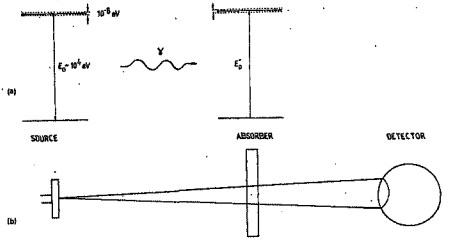


Fig. 2.1.1 (a) The γ-ray resulting from nuclear decay in a free nucleus and the corresponding nuclear absorption by an identical nucleus. E_o must match E_o' to within 10^{-8} eV for the process to occur. (b) A schematic of the setup used to measure nuclear absorption of γ-rays.

(see *fig. 2.1.1 (b)*). The number of γ-rays transmitted $N(v)$ as a function of velocity is given by Kolk (1984, p. 181)

$$N(v) = N_\infty - \varepsilon(v)N_\gamma, \qquad (2.2)$$

where N_∞ is the number transmitted at high velocities far from resonance (i.e. the base line value), N_γ is the number of γ-rays emitted by the ME transition and $\varepsilon(v)$ is the fraction of N_γ absorbed recoil-free at velocity v. For a thin absorber $\varepsilon(v)$ is given by

$$\varepsilon(v) = \frac{f_S f_a n \sigma_o (\Gamma_m/2)^2}{(v - v_o)^2 + (\Gamma_m/2)^2} \quad , \qquad (2.3)$$

where $\Gamma_m = 2\pi c/E_o$ is the full width at half maximum of the resonance line in velocity units, f_S and f_a are the recoilless fractions of the source and the absorber respectively, n is the number of resonant nuclei per unit area and σ_o is the maximum absorption cross section. $N(v)$ is at minimum when $\varepsilon(v)$ is at maximum, that is at $v = v_o$. Various interactions of the nuclear moments with the environment can cause the absorption line to be shifted or split into a number of lines.

2.2 The isomer or chemical shift.

The Coulomb interaction between the electronic charge present at the nucleus and the charge distribution of the nucleus produces a small shift in the transition energy E_o called the isomer shift, δ. This is measurable only when the non-relativistic electron density at the nuclear site, ρ (also known as the contact density), of the source and absorber is not identical. In velocity units, the isomer shift is given by Greenwood (1971, p. 49)

$$\delta = (2/3)(\pi c/E_o) Z e^2 \Delta\langle r^2\rangle \Delta\rho(0) \quad , \qquad (2.4)$$

where $\Delta\langle r^2\rangle$ represents the change in the second moment of the nuclear charge distribution between nuclear excited and ground states, $\Delta\rho(0) = \rho$(absorber) - ρ(source). Equation (2.4) must be multiplied by a relativistic correction factor $S'(Z)$ which is a function of the atomic number Z, (Kolk 1984, p. 22). The dominant contribution to the contact density arises from the s electrons. The isomer shift reflects the difference in the outer s electron configuration between atoms in the source and the absorber. In addition non-s electron distributions can also indirectly affect $\Delta\rho(0)$ through the screening of s electrons. Experimentally, the shift in the centroid of the resonance pattern constitutes the isomer shift.

2.3 *The magnetic dipole interaction.*

The interaction of the nuclear magnetic dipole moment with the magnetic field H at the nucleus is described by the Hamiltonian

$$\mathcal{H} = -\vec{\mu} \cdot \mathbf{H}. \qquad (2.5)$$

This interaction causes a nuclear state to split into $2j + 1$ substates with energies

$$\Delta E(j,m) = -\mu H m/j \qquad (2.6)$$

taken with respect to the energy of the unperturbed state, where j is the nuclear spin and m is the magnetic quantum number; note that $|m| \leq j$.
The ME spectrum reflects transitions between various excited and ground state subleveis (*fig. 2.3.1*) which for dipole radiation must obey the selection rule $|m_e - m_g| = 1$ or 0, where m_e and m_g are the magnetic quantum numbers of the excited and ground states respectively. The magnetic hyperfine field at the *nucleus deduced from the Mössbauer spectrum* allows us to study the magnetic behavior of the material.

2.4 The electric quadrupole interaction.

Nuclei with spins greater than $\frac{1}{2}$ have quadrupole moments eQ that can interact with the electric field gradient (EFG) at the nucleus. The quadrupole moment is related to the shape of the nucleus. The EFG is a tensor with nine components $V_{xy} = \partial^2 V/\partial x \partial y$ etc., where $V(x,y,z)$ is the potential at a point (x,y,z). *By choosing a proper* set of axes (principal coordinates) the off-diagonal elements of this tensor can be made zero. Usually one defines this axis system so that the EFG is a maximum in the z direction. and the modulus of the quantity eq is the maximum value of the EFG.

The quadrupole interaction can partially lift the degeneracy of the nuclear states involved in the Mössbauer transition. The various substates have energies differing from the unperturbed nuclear state by an amount (Kolk 1984, p. 29)

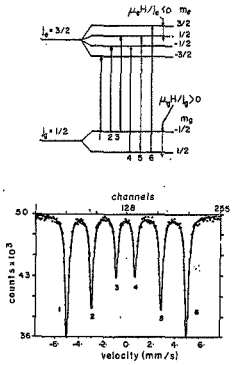


Fig. 2.3.1 (Top) The allowed nuclear transitions when the excited state and the ground state are split due to the magnetic hyperfine field. (Bottom) Note the decrease in transmission at each of the allowed nuclear transitions as reflected in the ME spectrum obtained using ^{57}Fe Mössbauer nuclei, with iron foil as the absorber and ^{57}Co in rhodium as the source.

$$\Delta E(j,m) = e^2qQA(j,m,\eta). \qquad (2.7)$$

The quantity η is related to the symmetry of the EFG and is called the asymmetry parameter. For axial symmetry ($\eta = 0$)

$$A(j,m,0) = \frac{3m^2 - j(j+1)}{4j(2j-1)}. \qquad (2.8)$$

Recall $|m| \leq j$ where each m corresponds to a different orientation of the nucleus. Equations (2.7) and (2.8) indicate that the interaction energy between a nucleus and the EFG is different for each possible orientation of the nucleus. This results in a so-called *quadrupole splitting of the ground and/or excited states*. For the important case of $j = 3/2$,

$$A(3/2,m,\eta) = A(3/2,m,0)(1 + \tfrac{1}{3}\eta^2)^{\frac{1}{2}}. \qquad (2.9)$$

Thus for $j_e = 3/2$ and $j_g = 1/2$, where the subscripts refer to the excited and ground states respectively, the ME spectrum will show two absorption lines at the velocities

$$v_{1,2} = \delta \pm \tfrac{1}{4}e^2qQ_e(c/E_\gamma)(1 + \tfrac{1}{3}\eta^2)^{\frac{1}{2}}, \qquad (2.10)$$

where Q_e refers to the quadrupole moment of the excited nucleus. *Fig. 2.6.1* shows the corresponding nuclear transitions involved. The knowledge of the EFG primarily reflects the lattice symmetry at the lattice site of the Mössbauer atom.

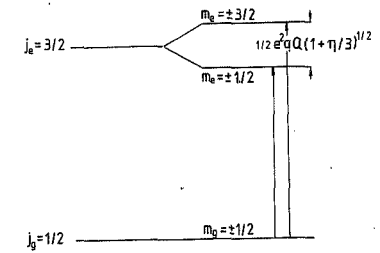


Fig. 2.4.1 Quadrupole splitting for a spin 3/2 → 1/2 transition.

2.5 The recoilless fraction.

In the semi-classical picture of a solid the atoms are connected to one another by springs to form a regular lattice structure. The recoil of a nucleus emitting a γ-ray may excite the spring system -- lattice vibrations. However, the vibrational energies are quantized and are known as phonons. It is possible that the recoil energy E_R transferred to the lattice is not able to create phonons. In such a zero phonon process the recoil is taken up by the total mass of the lattice resulting in negligible recoil. There is thus a finite probability for *recoilless γ-ray emission or absorption by a nucleus embedded in a solid.* By definition the fraction f of γ-rays emitted without transfer of recoil energy to the vibrational states of the lattice is called the recoilless fraction. The f value depends on the free-nucleus recoil energy, which is proportional to E_γ^2, where E_γ is the energy of the γ-ray, and the properties of the lattice which change as

a function of temperature. The following indicates how a study of the temperature dependence of the recoilless fraction provides a valuable means of studying the lattice dynamical properties of a solid.

The probability that the lattice remains in the same state when a γ-ray is emitted or absorbed, that is, that no phonons are created or absorbed is (Kolk 1984, pp. 65-66)

$$f = exp\ [-k^2\ \langle x^2 \rangle_T] \ , \qquad (2.11)$$

where $\langle x^2 \rangle_T$ is the projection of the mean-square displacement of an atom along the direction of the wave vector k of the γ-ray. This relation between f and the mean-square displacement establishes a connection between the recoilless fraction and the lattice dynamics. For a thin absorber the area under a single line Mössbauer spectrum is related to the recoilless fraction by (Vertes et al. 1979, pp. 30-33)

$$A = n_a f_a \ , \qquad (2.12)$$

where n_a is the number of resonant nuclei per unit area in the absorber. The area is given by the product of the measured linewidth and the intensity normalized to the intensity far off resonance. Dividing by the natural line width makes the area a dimensionless quantity.

For atoms moving in parabolic potentials (*harmonic approximation*), the motions of the individual atoms are described by the superposition of $3N$ independent modes. In a real crystal, interactions between atoms mean that the interatomic potentials may deviate from being parabolic. This adds anharmonic terms to the vibrational Hamiltonian. The anharmonic terms and their associated anharmonic effects are responsible for the lattice properties of a crystal, for example, thermal expansion and temperature dependence of the elastic constants. To account for the anharmonic effects the temperature dependence of the recoilless fraction is examined in the *pseudo-harmonic approximation*. Here the thermal expansion of the lattice and the interactions between phonons are taken

into consideration. This approximation is valid for cases where the interatomic potentials are nearly parabolic as is the case in most solids. To expose the anharmonic effects the recoilless fraction data is separated into two groups : data measured at moderate and high temperatures $T \geq \theta_{-2}/2\pi$ and data measured at $T \leq 5$ K, (Kolk 1984, pp. 68-71). θ_{-2} is a so-called harmonic characteristic temperature defined by

$$\theta_n = \frac{\hbar}{k_B} \left[\frac{1}{3}(n+3) \frac{1}{3N} \int_0^\infty \omega^n g(\omega) d\omega \right]^{1/n}, \qquad (2.13)$$

where $g(\omega)$ is the phonon spectrum of the solid and N is the number of atoms. From equation (2.13) it follows that for a Debye solid $\theta_n = \theta_D$ for all n, where θ_D is the Debye temperature. The anharmonic counterpart of θ_n is defined by

$$\theta_n^a(T) = \theta_n [\, 1 - \varepsilon(n) T + \ldots \,] \qquad (2.14)$$

to first order, where $\varepsilon(n)$ is the anharmonic constant of order n.

For $T \geq \theta_{-2}/2\pi$ the data can be fitted by the following equation (Kolk 1984, §2.6)

$$-\ln f(T) = k^2 \langle x^2 \rangle_T = \frac{6E_R}{k_B} \frac{T}{\theta_{-2}} \left[1 + 2\varepsilon(-2) T + \left(\frac{\theta_{-2}}{6T} \right)^2 + \ldots \right], \qquad (2.15)$$

where E_R is the recoil energy of a free atom. Higher order terms in equation (2.15) are negligible. When $\varepsilon(-2)$ equals zero we have the *harmonic approximation*. The quantities θ_{-2} and $\varepsilon(-2)$ can be obtained from a least squares fit of the data. For impurities in a lattice, θ_{-2} permits the evaluation of the impurity force constant. The constant $\varepsilon(-2)$ yields information on the anharmonic terms in the vibrational Hamiltonian.

For $T \leq 5$ K, the recoilless fraction is given by

$$-ln\ f(T) = k^2\langle x^2\rangle_T = \frac{3}{2}\frac{E_R}{k_B}\frac{1}{\theta^{\theta}_{-1}(T)} \quad . \tag{2.16}$$

The characteristic temperature $\theta^{\theta}_{-1}(T)$ enters in the expression for the electron-phonon coupling constant related to the T_c of a superconductor (Kolk 1984, §2.6).

Equations (*2.15*) and (*2.16*) indicate that recoilless fraction measurements serve as a unique way of studying the lattice properties.

3. THE MÖSSBAUER SPECTROMETER

3.1 Introduction

The general method of utilizing the ME is to measure the transmission of γ-rays emitted by a source through an absorber as a function of the source velocity v relative to the absorber. The variation of the γ-ray energy with v is given by the Doppler equation

$$E_\gamma = E_o(1 + \frac{v}{c}), \qquad (3.1)$$

where E_o is the nuclear transition energy transferred to the γ-ray. In our case the transmission of 23.875 keV γ-rays through an absorber containing ^{119}Sn is measured. The recoil-free γ-ray energy of a typical Mössbauer transition is Doppler modulated by an electromechanical system operated in the constant acceleration mode. At a particular velocity the γ-ray energy from the source precisely matches the nuclear energy level in the absorber and resonant absorption will occur. As mentioned *in chapter 2, a degenerate energy level in the* absorber splits into more than one level due to electric field gradients or internal hyperfine magnetic fields. In that case resonant absorption and a decrease in transmission of γ-rays occurs at more than one velocity. Therefore a plot of the intensity of the transmitted γ-rays against the velocity of the source yields direct information about the energy levels in the emitting or absorbing nuclei.

In the transmission geometry it is easier to move the source and keep the absorber (sample) stationary. This makes it easier to change absorbers and vary their temperature. A schematic of the ME spectrometer used in transmission geometry for studies at low temperatures is shown in *fig. 3.1.1*. The main components are, the electromechanical drive system that imparts a velocity to the source, the multi-channel analyser (MCA) used for counting the number of transmitted γ-rays as a function of the source velocity, the detection system for

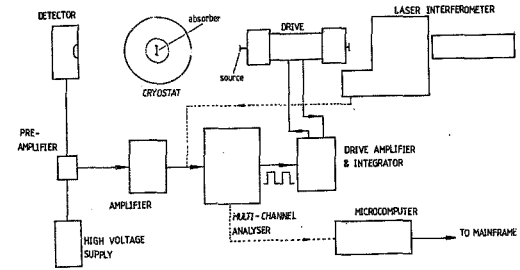


Fig. 3.1.1 An overview of the low-temperature ME facility for use in the transmission geometry.

recording the transmitted γ-rays and the cryostat in which the absorber is kept and cooled to some low temperature.

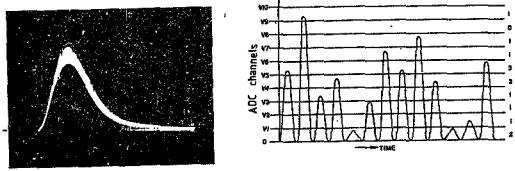
3.2 The Multi-channel Analyser.

An important feature of the ME spectrometer is the (multi-channel analyser) MCA which performs data acquisition and synchronization. It can be operated in two basic modes.

(*a*) *Pulse Height Analysis Mode.* In the most common application of pulse height analysis (PHA), a detector is placed near a radioactive source. The detector produces a voltage pulse whose amplitude is proportional to the energy of the incident radiation. *Fig. 3.2.1* (*a*) is a photograph of voltage pulses as they might appear at the output of an amplifier.

The stream of pulses is then fed to the Analog-to-Digital Converter (ADC). The ADC divides the total range of the input voltage into a number of discrete intervals called ADC channels. Referring to *fig 3.2.1* (*b*), the column of numbers on the right indicates the number of pulses falling into each ADC channel. For each pulse which falls within a specific voltage interval (corresponding to a specific energy interval), one "count" is tallied in the corresponding data memory storage location or channel. There exists a one to one mapping of ADC channels to data memory channels. Examples of PHA spectra are shown in *figures 5.2.2 and 5.2.3*. A radioactive isotope produces a characteristic and readily identifiable spectrum of this type. Each point in the spectrum represents the counts tallied in a single data channel ; each channel represents a voltage (energy) interval. The use of the PHA mode in the Mössbauer spectrometer will be explained below.

(*b*) *Multi-channel scaling mode.* In the multi-channel scaling (MCS) mode the input pulses, each of which represents a specific event (for example, the detection of a γ-ray), are measured as a function of time. MCS operation effectively employs the data memory as a series of scalars (pulse counters). As the pulses are detected at the MCS input, they are counted in a high-speed register for a preset interval (dwell time). At the end of each interval the value in the scalar is added to the contents of the current memory channel and the scalar is cleared and advanced for the next dwell interval; the value of the scalar for this next dwell time will be added to the next channel, and so on. When pulses have been tallied in all of the channels, a "sweep" has occurred; the beginning of the next sweep starts at the first channel, and the above sequence of events is repeated. This continues until a sufficient number of counts have been acquired in each channel.



(a) (b)

Fig. 3.2.1 (a) A photograph of pulses from a $CaSnO_3$ source as they appear at the output of an amplifier. (b) The ADC process.

For use in Mössbauer studies, the MCS scan is synchronized with the motion of an electromechanical drive. The channels of the MCS spectrum are then directly related to the velocity of a source attached to the drive system.

The statistical behavior of the γ emission results in a standard deviation of $\sqrt{N}$ for a total N of registered γ counts per channel. Hence the longer the counting time, the better the definition of *the resonance line; but the improved* resolution to be gained must be balanced against the experimental time available and the long-term stability of the apparatus.

3.3 The electromechanical drive system.

The Doppler shift of the source is provided by an electromechanical drive system (Austin Science Associates K3 linear motor) which is controlled by a *home-built drive amplifier* (Corson 1980). The amplifier is fed with a reference voltage waveform from the MCA which has a frequency of 5 Hz. The actual drive or transducer embodies two coils, one of *which produces a voltage proportional* to the actual velocity of a center shaft. The drive amplifier compares this signal

to the reference waveform via negative feedback and applies corrections to the drive coil to minimize any differences. In this way the Mössbauer source attains a velocity which precisely tracks the reference wave form.

A square wave signal is taken from the MCA and integrated to yield a triangular waveform (linear velocity, constant acceleration) which is used as the reference voltage. The symmetrical triangular waveform causes a velocity scan of the spectrum with constant acceleration in opposite directions, alternately. This produces a double (mirror-image) spectrum. The linearity and stability of our drive system is improved significantly over that of conventional drive systems by using a correction signal in addition to the negative feedback (for details see Corson 1980). The velocity is varied linearly up to a maximum of approximately 10 mm/sec.

3.4 Detection Equipment.

The ɣ-ray detection system used in ME experiments is made up of a detector, preamplifier, main amplifier and a discriminator. In our experiment two different types of detectors were used : a proportional counter and a planar germanium detector.

The proportional counter is a gas-filled outer casing with a central electrode. The initial reaction between radiation which enters and the gas in the counter, is the photoelectric effect. In the detector a large potential difference applied across the positive central electrode and the outer casing prevents recombination of the liberated electrons and ions, and the electrons are attracted to the positive electrode. The charge sensitive preamplifier generates an output voltage proportional to the charge resulting from ionizing events, and therefore proportional to the deposited energy. These output voltages (pulses) are directed to the ADC via the linear amplifier. PHA mode then allows us to examine the energy spectrum of the ɣ-ray source.

In high purity germanium detectors, electron-hole pairs are produced by an ionizing event in a semiconductor (Ge) crystal. When a ɣ-ray is absorbed, the number of carriers produced by ionization is linearly related to the energy absorbed. Only a small amount of energy (≤ 1eV) is required to produce an

electron-hole pair; so the number of carriers produced for a given energy is large, and the statistical fluctuations in that number are small when expressed as a percentage of the total number. The statistical fluctuation of the number of carriers N produced when a γ-ray is absorbed is $1/\sqrt{N}$. The extent of this statistical fluctuation accounts for the resolution of the detector. This type of detector gives much better energy resolution than that of a proportional counter as can be seen by comparing *figures 5.2.2* and *5.2.3*. *Fig. 5.2.2* is a pulse height spectrum of a ^{119}Sn $CaSnO_3$ source. This was obtained with a xenon-methane filled proportional counter operated at a stable voltage of ~ 2750 volts. *Fig. 5.2.3* shows that the lines are better resolved when a pulse height spectrum of the source was recorded with our germanium detector. This detector consists of a circular cylinder of intrinsic Ge with a built-in pre-amplifier and high voltage supply. Usually Ge-type detectors have to be kept at liquid nitrogen temperature. However an intrinsic Ge detector can be cycled between room temperature and liquid nitrogen as often as is necessary. Before use, the detector has to be cooled and this is repeated every twelve hours for the duration of the measurement. The high resolution of this detector is required for accurate recoilless fraction measurements where there is a need for the determination and subsequent elimination of the background radiation, that is, radiation not resulting from the Mössbauer transition but having comparable energy due to various processes (for example, scattering or the "tail" of an adjacent x-ray line).

After viewing the pulse height spectrum in PHA mode a window is set with the discriminator which allows only the γ-rays of interest to be recorded in the MCS mode. When the discriminator has been set and with the MCA in MCS mode, the spectrometer is ready for use.

3.5 Velocity Calibration.

In order to assign velocities to each channel in a Mössbauer spectrum we require some means of velocity calibration. A calibration is performed before and after a Mössbauer spectrum is acquired. The conventional technique involves recording a ^{57}Fe ME spectrum of a natural iron foil with a single line ^{57}Co source.

The ME spectrum exhibits six absorption lines, the positions, and therefore velocities, of which are accurately known.

We use a more accurate method for calibrating the spectrum. This involves an optical technique that uses the principles of a Michelson-interferometer. A schematic diagram of the Michelson-interferometer as implemented in a velocity calibration system is shown in *fig 3.5.1*.

The principle of operation is as follows : whenever the drive moves a distance $\lambda/2$, where λ is the wavelength of the laser light, a light and a dark fringe ss the photodetector. The fluctuating light signal is converted into pulses so that in a fixed time interval the number of pulses is proportional to the displacement of the drive. The pulses are fed into the multi-channel analyzer (MCS mode), and the number of pulses counted in a fixed time gives the velocity corresponding to that channel. This is clear from the fact that if each channel is open for the dwell time τ then the velocity corresponding to channel x, v_x, is

$$v_x = N_x \frac{\lambda}{2} \frac{1}{P\tau} \qquad (3.2)$$

where P is the number of sweeps and N_x is the number of counts (number of half wavelengths traversed). The average velocity associated with each channel is accurately determined. *Fig. 3.5.2* is a velocity calibration spectrum. The number of fringes passing the detector is a measure of $|v|$ and this accounts for the inversion of the triangle in the calibration spectrum.

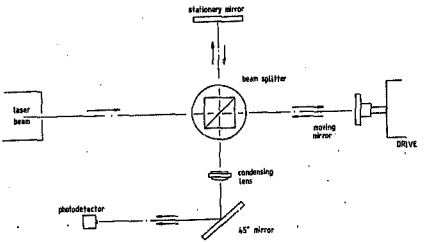


Fig. 3.5.1 Velocity calibration system.

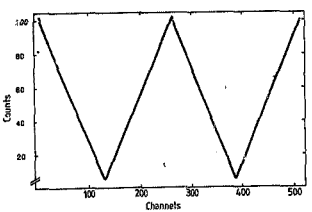


Fig. 3.5.2 *A velocity calibration spectrum. The counts in each channel represent the velocity associated with that channel.*

4. THE LOW TEMPERATURE APPARATUS

4.1 The Cryostat.

Low temperatures are obtained in a Janis stainless steel cryostat. A schematic of the cryostat is shown in *fig. 4.1.1*. A vacuum jacket thermally isolates a liquid nitrogen reservoir from the surroundings. The liquid nitrogen reservoir encapsulates a liquid helium reservoir. When filled with liquid nitrogen this arrangement decreases radiational heating that leads to an increase in the rate of consumption of liquid helium. The helium reservoir surrounds the sample tube into which the sample holder is inserted. Attached to the top of the sample holder is a sample positioner for locational control of the sample and two electrical feedthroughs to allow access of electrical equipment such as a thermocouple, a temperature controller resistance sensor and a resistor for temperature measurements.

At the end of the sample holder, in close proximity to the sample mount, is a 25 ohm bifilar wound non-magnetic heater used in conjunction with a temperature controller to allow temperature stabilization of the sample. There is also a mounting provision for a highly reproducible temperature sensing Carbon Glass Resistor. Also attached to the end of the sample tube is a 25 ohm bifilar wound non-magnetic vaporizer heater that is used to vary the temperature in the sample tube.

The sample tube has a vapor pumping port to which a mechanical pump is connected through a connecting line. Pumping on liquid helium that has condensed at the bottom of the sample tube allows us to obtain temperatures as low as 1.5 K. A needle valve permits controlled flow of liquid helium into the sample tube from the helium reservoir thus allowing the sample to attain reduced temperatures.

The cryostat was mounted on a specially constructed table by means of a mounting flange. A wooden base is coupled to a metal frame by means of shock absorbers and this combination forms a table like support. Shock absorbers are

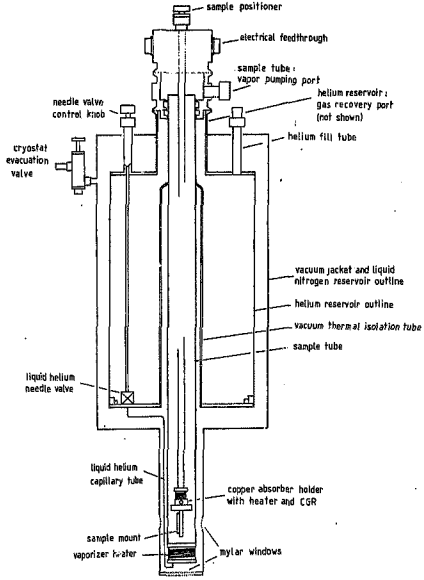


Fig. 4.1.1 A schematic diagram of the Janis Mössbauer cryostat.

also attached to the legs of the table. The shock absorbers nullify the effect of vibrations on the cryostat due to mechanical pumps, air conditioning units and compressors. Vibrations cause spectral line broadening which can mask the effect of hyperfine interactions. A Zeolite pump is attached to the table and is used

for the evacuation of the outer jacket of the cryostat. A plan view of the setup is shown in *fig. 4.1.2 (a)* and a side view is shown in *fig. 4.1.2 (b)*.

The mylar windows indicated in *fig. 4.1.1* allow transmission of γ rays. They are vacuum sealed and have a low absorption coefficient for the γ rays of interest. The windows are situated so that vertical or horizontal transmission of γ rays is allowed. If the source has a high recoilless fraction at room temperature it can be situated outside the cryostat and the horizontal transmission geometry is suitable. Vertical transmission geometry is used when the source has to be maintained at a low temperature to increase the recoilless fraction. The cryostat is supported above a hole in the floor, of dimensions one meter squared, to allow the vertical transmission geometry. Our source exhibits a high recoilless fraction at room temperature as judged from the percentage effect observed (~ 20 %) when a room temperature spectrum was recorded. We are thus able to use the cryostat in horizontal transmission geometry. The drive and velocity calibration systems were mounted on jacks, the heights of which could be varied to maximize transmission through the mylar windows and absorber. The drive and velocity calibration system were first mounted on foam rubber supports to dampen vibrations.

Fig. 4.1.3 shows a gas distribution facility and mechanical vacuum pump used for recovery of ^{4}He gas and to allow pumping on liquid ^{4}He to obtain temperatures as low as 1.5 K. The facility has inlets from the storage dewar, cryostat helium reservoir and sample tube. All recovered helium gas is recorded on a gas meter and is directed to the central recovery system. In cases where the mechanical pump is used to pump on liquid helium, the resulting oil-helium gas mixture is directed through an oil filter to extract the helium gas.

Before cooling, the absorber is mounted on the sample holder and inserted in the cryostat. Starting up procedures involve evacuating the outer jacket of the cryostat to ~10^{-5} Torr. The liquid nitrogen reservoir is then filled and the cryostat is left to cool overnight. The liquid nitrogen level is maintained above the liquid helium reservoir by an automatic filling system. The filling system incorporates a cryogenic level detector and associated electronics designed and built in the Mössbauer laboratory. The level detector consists of a length of

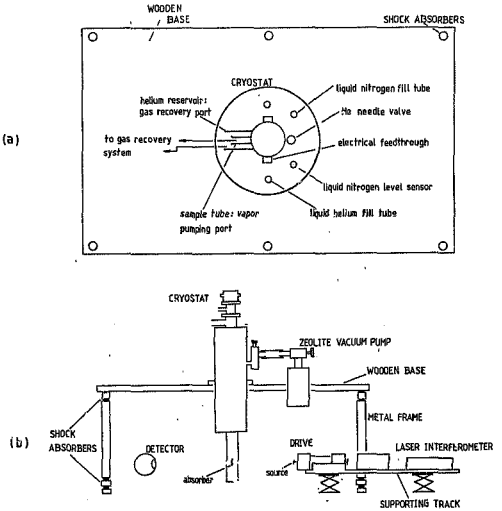


Fig. 4.1.2 The experimental setup as viewed from (a) above, (b) the side.

hollow teflon tubing (low thermal conductivity) into which two Allen Bradley carbon composition resistors are fixed. Their resistance changes by orders of magnitude when the temperature is changed from ambient to 77 K (liquid nitrogen). This property serves as a triggering mechanism enabling the resistors to be used as "high" and "low" level sensors. When the liquid nitrogen level drops below the "low" level sensor a compressor is triggered to pressurize a liquid nitrogen storage dewar. The nitrogen reservoir of the cryostat is filled until the "high" level sensor triggers.

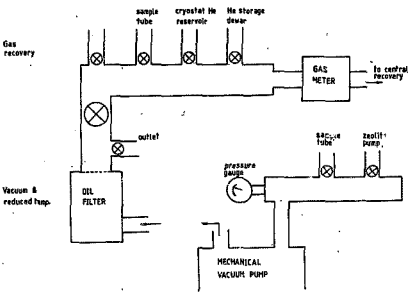


Fig. 4.1.3 The gas distribution facility and pumping system used for He recovery and used to achieve temperatures as low as 1.5 K.

The helium reservoir is then manually filled from a storage dewar with the aid of a flexible transfer tube. The vacuum gauge and gas meter are monitored closely during the filling. An initial fast tempo of the gas meter indicates a significant boil off of helium due to cooling of the helium reservoir. Upon condensation of helium in the reservoir, the vacuum is reduced to below 10^{-6} Torr. The maintenance of this vacuum and a reduction in the boil-off rate as indicated by the gas meter, *signals helium accumulation* in the reservoir. Normally the five litre helium reservoir is filled to approximately 80 % capacity sufficient to last 24 to 36 hours (*fig. 4.1.4*). The level of the *liquid helium* is measured with a dipstick. The needle valve connecting the helium reservoir to the sample tube is then opened to allow liquid helium flow into the sample tube. In this way the absorber is cooled to liquid helium temperature, 4.2 K. The cooling rate in the sample tube can be varied. A needle valve attached to the *vapor pumping* port allows one to change the speed at which vapor is pumped off liquid helium that has condensed at the bottom of the sample tube.

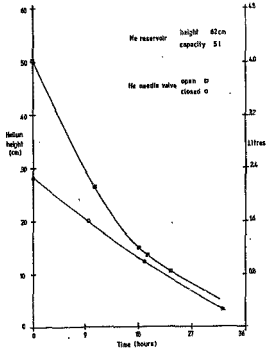


Fig. 4.1.4 He consumption in the cryostat.

In summary, important features of the cryostat are

(1) the temperature of the sample is easily varied between 4 K and 300 K by means of vaporizer heater power,

(2) pumping on ^{4}He that has condensed in the sample tube allows one to obtain temperatures as low as 1.5 K,

(3) the construction of the cryostat allows one to maintain either the source or the absorber or both at low temperatures. This is necessary depending on the characteristics of the source, and

(4) the sample can easily be changed.

4.2 Temperature control and stability.

Allen Bradley (AB) carbon composition resistors were used as temperature sensors. A 479 ohm AB resistor was used as the sensor for a temperature regulator and a 74 ohm AB resistor was used to measure the temperature. Both resistors were calibrated at 300 K, 77 K and 4.2 K prior to performance of experimental runs. The low temperature points were obtained by immersing the

resistors in cryogen storage dewars and recording the resistor values on a hand-held digital multimeter. The calibration curves are shown in *fig. 4.2.1.*

In order to maintain stability at low temperatures, a temperature regulator was built. The regulator was modelled after that of Newrock, Wagner and Rosenthal (1977). The regulator was operated with the 479 ohm AB resistive sensor whose resistance-temperature behavior is shown in *fig. 4.2.1.* It can also be operated with a capacitive sensor which is unaffected by the application of magnetic fields.

A block diagram of the regulator is shown in *fig. 4.2.2.* The sensor (resistor R_S) and heater (resistor R_H) are required to be in good thermal contact with the sample mount. The resistive sensor was securely attached with copper wire on the sample mount adjacent to the sample. The 25 ohm heater close to the sample holder was used as R_H. The temperature control point is determined by the resistance of R_D. Depending on the sensor temperature relative to the control point, an error signal at the oscillator frequency is produced at the output of the active bridge. The active bridge yields an output that is linearly related to the input voltage and to the difference between R_S and R_D. An appropriate component of this signal is phase detected, and the output after filtering is applied to the heater.

The phase sensitive detector circuit is built as part of the regulator avoiding the need for a costly commercial phase sensitive detector in the feedback loop. The phase shifter is only used for controller operation with a capacitive sensor. The gain and time constant of the regulator is adjustable to optimize its operation.

The control point (R_D) was set at a temperature higher than that at which the measurement was to be performed. By maintaining a constant cooling rate, a constant current is supplied to the heater to offset the cooling and equalize R_D and R_S, the control point temperature and the sample temperature, respectively. Operated in this way, a heater current of approximately 20 mA is regulated, thus stabilizing the temperature of the sample. The maximum allowed heater current is 120 mA and is low enough to allow minimal power input into the sample zone. The alternative way of using the regulator is to allow R_D and R_S to equalize so that the heater current is regulated about a zero value. This

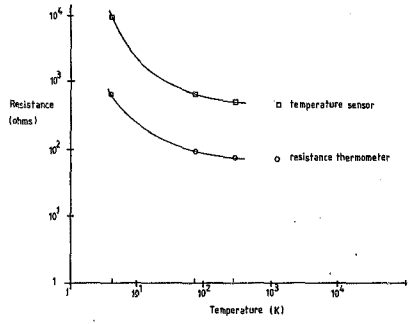


Fig. 4.2.1 Calibration curves of the resistors used for temperature control and measurement.

effectively means regulating the cooling of the sample which is difficult because of temperature gradients and temperature fluctuations in the sample tube. The 74 ohm AB resistor used to monitor the temperature was securely attached to the sample mount in close proximity to the sample. Resistance values were read off a digital multimeter.

For measurements at 22 K and below the 74 ohm AB resistor showed a drift of less than 0.5 ohms over a 24 hour period. This corresponds to a temperature stability of 100 mK at 22 K and better at lower temperatures. Temperatures between 77 K and 120 K drifted by 2 K about the measuring point in the worst case. Above 150 K the temperature drifted as much as 5 K about the measuring point. The decrease in stability at the higher temperatures is due to the lack of sensitivity of R_S to changes in temperature above 77 K. This can be overcome by using a resistor with greater sensitivity in the higher temperature range.

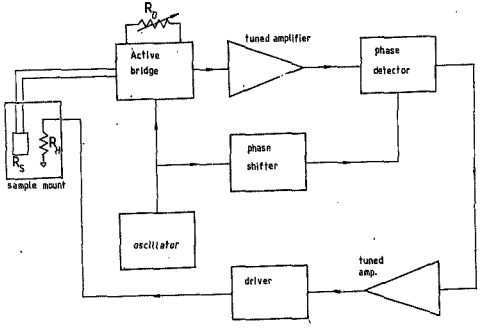


Fig. 4.2.2 A block diagram of the temperature regulator.

5. MOSSBAUER EFFECT STUDIES ON NB-SN COMPOUNDS

5.1 Introduction

Technologically, superconductors with high transition temperatures and high upper critical fields have the most practical value. The operating temperature range is more accessible and they can produce and tolerate high magnetic fields. An example is the type II superconductor Nb_3Sn with $T_c \sim 18.05$ K and $H_{c2} \sim 22$ T ; it has one of the highest known transition temperatures. This material is of technological use in the construction of high field, low power consumption, superconducting magnets.

Superconducting tape is synthesized using tin wire and niobium with the intention of obtaining a Nb_3Sn layer. Recent work of Glowcki and Chojchan (1983) indicates a dependence of the layer phase composition on the method of preparation, that is, on such parameters as the wetting and annealing temperatures. Ideally one would require that the superconducting layer consist almost entirely of the β-Nb_3Sn phase but from the Nb-Sn phase diagram, *fig. 5.1.1*, it is evident that the more undesirable Nb_6Sn_5 and $NbSn_2$ phases, and Nb-Sn solid solutions may be obtained.

^{119}Sn ME spectroscopy is a non-destructive method of studying the phase composition of the Nb-Sn layers in Nb-Sn superconducting tape. Such a phase analysis has been performed by Growcki and Chojchan (1983), and Sitek et al. (1978). We followed the evolution of the ^{119}Sn Mossbauer spectrum of commercial Nb-Sn tape from 300 K down to 4.2 K using the low temperature facility described in the previous chapter. Besides studying the phase composition of Nb-Sn superconducting tape, we have investigated the mean-square displacement of Sn atoms in the various phases. This allows us to look for possible correlations between the lattice properties and T_c which is different for each phase.

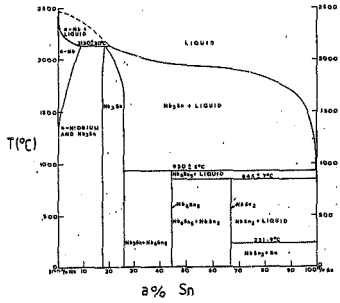


Fig 5.1.1 The phase diagram of the Nb-Sn system. (Figure taken from Charlesworth et al. 1970.)

PHASE	Nb_3Sn	$NbSn_2$	Nb_6Sn_5	β-Sn
T_c (K)	18.05	2.60	—	3.72
CRYSTAL STRUCTURE	A15	ORTHORHOMBIC	ORTHORHOMBIC	TETRAGONAL B.C.

Table 5.1.1 The crystal structure and superconducting transition temperature of various Nb-Sn compounds (from the CRC Handbook of Chemistry and Physics, 60th edition).

5.2 The ^{119}Sn source.

For ^{119}Sn Mossbauer studies, the 23.875 keV γ-ray used arises from a decay of the first excited state, which is populated by a decay of metastable ^{119m}Sn with a half-life of 245 days. The decay scheme of ^{119m}Sn is shown in *fig. 5.2.1.* The ^{119m}Sn is formed by neutron irradiation of ^{118}Sn. The excited state half-life of 17.86 ±0.10 ns corresponds to a natural line width of $\Gamma_o = 0.642(4)$ mm/s, and the decay to the ground state is a 3/2 → 1/2 magnetic dipole transition. The 23.875 keV γ-ray is rather highly internally converted. The 65.66 keV γ-ray is even more strongly converted and is consequently weak in intensity. The internal conversion process associated with the 65.66 keV decay results in 25.04 keV and 25.27 keV x-rays.

In order to study the hyperfine interactions we require a source which efficiently emits recoilless radiation of narrow spectral line width. Desirable features like a high recoilless fraction at room temperature together with a narrow line width are attained in the alkaline earth metal stannates ($MSnO_3$) due to the high symmetry of the perovskite structure. We use a $CaSnO_3$ source which meets the above requirements for high resolution Mossbauer spectroscopy.

A pulse height spectrum of the source taken with the proportional counter shows unresolved lines that include the Mossbauer γ-ray line, *fig. 5.2.2.* It is necessary to identify all lines that coincide with the Mossbauer γ-ray transition, thus contributing to background radiation. This is important in the case of recoilless fraction measurements where the background component has to be accurately known. To investigate the origin of the background radiation, we took a pulse height spectrum of the source (*fig. 5.2.3*) with the high resolution germanium detector. This spectrum shows the γ-ray lines indicated in the decay scheme above, and reveals additional x-ray lines. One of these lines can be attributed to x-rays from niobium present in the absorber. Other x-ray lines indicate that strontium and selenium are present in the source and may be a result of the preparation procedure. The tin x-ray lines are a result of the internal conversion processes in the source. The tin lines are preferentially absorbed with a palladium filter inserted between the absorber and the detector. Palladium

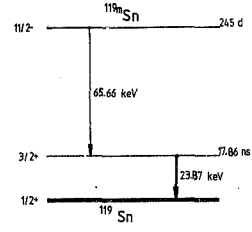


Fig. 5.2.1 The nuclear decay scheme of the ^{119m}Sn Mössbauer isotope.

has a K-edge for photoelectric absorption at 24.35 keV, intermediate between the unwanted x-rays and the important 23.875 keV Mössbauer transition.

5.3 Setting up a Mössbauer measurement.

We have acquired a few grams of superconducting tape which is approximately 100 microns thick and 0.5 cm wide. An Nb-Sn layer was made by diffusing niobium powder into tin tape and reacting; this was then sandwiched between two copper layers. The Nb-Sn layer is likely to consist of a mixture of phases that includes the high T_c $NbSn_3$ phase. A number of strips, approximately 2 cm x 0.5 cm, were overlapped to form a foil-like absorber of area 2 cm x 2 cm. This was then attached to the sample holder.

After lowering the temperature of the sample to 4.2 K, the temperature is raised to a desired value by means of vaporizer heater power. The vaporizer heater is energized by a regulated power supply. The temperature of the sample is known by monitoring the 74 ohm AB resistor. When the temperature is close to the value at which the measurement is to be performed the temperature con-

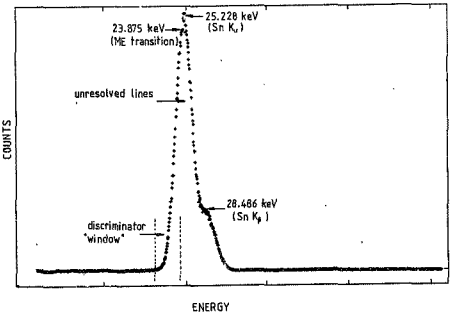


Fig. 5.2.2 A proportional counter pulse height spectrum of the source.

troller is switched on and the sample temperature zone is allowed to stabilize for an hour or two.

With the spectrometer and sample in position, a pulse height spectrum is recorded with a xenon-methane filled proportional counter. The discriminator window is set to eliminate as much of the background radiation as possible, *fig. 5.2.2.* The height and alignment of the spectrometer and the sample are adjusted to maximize the count rate. The discriminator is readjusted if necessary. The MCA is changed to MCS mode, the drive system is started and the measurement is allowed to run. The temperature is monitored as often as possible and recorded approximately every six hours for the duration of the measurement. A velocity calibration spectrum is run before and after every Mössbauer measurement. This is to check for any changes in the linearity of the drive system.

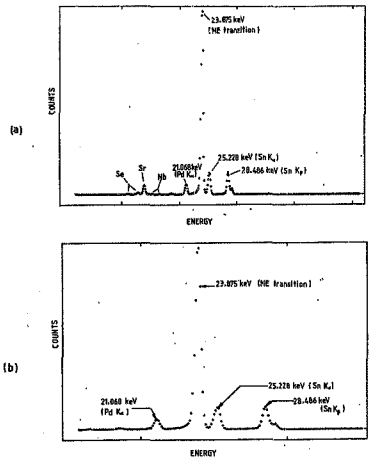


Fig. 5.2.3 (a) An Aptec Ge detector pulse height spectrum of the source showing most of the radiative transitions; a palladium filter was used. (b) A pulse height spectrum showing only the more important transitions. Compare this spectrum with that of fig. 5.2.2.

5.4 Data acquisition.

To achieve desirable statistics in a Mössbauer spectrum a sufficient number of counts has to be accumulated in each channel. The duration of a measurement depends on the source strength and the geometry of the setup. For sufficient statistics in our case where 2048 channels are used, 25000 counts per channel is required. With our 5 mCi $CaSnO_3$ source this means approximately 24 hours measuring time. The temperature controller was able to maintain the stability of the sample temperature during this time.

At the end of a measurement the data accumulated in the MCA was transferred to a DEC Rainbow microcomputer and stored on floppy disk. Data transfer between the MCA and the microcomputer complies with EIA standard RS232 communication protocols. The microcomputer is linked to an IBM/360 mainframe via a modem. The data on floppy disk is transferred to the mainframe by means of a POLY-XFR/TRM terminal emulation package. The full transfer operation takes of the order of a few minutes. On the mainframe the data is analyzed with the aid of a sophisticated computer program, MÖSSFUN (Müller 1980). Data analysis is described below. The velocity calibration spectra run before and after the Mössbauer spectrum are transferred to the mainframe in the same way and analyzed separately with the aid of the program LASERCAL. The output of this program issues important data for use in the analyzing routines of MÖSSFUN.

5.5 Data Analysis

The first step involves analyzing the laser calibration spectra. This is done with the aid of the program LASERCAL specially designed for this purpose. The calibration spectrum can be divided into four regions as indicated in *fig. 5.5.1*; the corresponding motion of the drive for each region is shown. LASERCAL fits a straight line to each of the four regions enabling us to find the velocity per channel for each region. This is important because any small non-linearity that occurs in one of the regions is immediately exposed and is not carried over to the other regions. The first half of the spectrum (regions *1* and *2*) and the second half (regions *3* and *4*) have 512 accurately determined calibration points. This should be compared with the conventional Fe foil calibration method in which only six calibration points are associated with each half. For this reason LASERCAL provides accurate values for the velocity per channel of four regions of a Mössbauer spectrum, the channel of zero velocity for each half and the folding point about which the spectrum is symmetrical.

A Mössbauer spectrum may be a superposition of sub-spectra each of which corresponds to the Mössbauer isotope in a different environment, *fig. 5.6.1*. The sub-spectra may thus represent different phases that are present in the absorber. For a thin absorber each sub-spectrum can be approximated by a

Lorentzian function (Kolk 1984, pp.181-182, 187). The theoretical fit to the overall spectrum is a sum of Lorentzians. Therefore the theoretical intensity F at the velocity v for a spectrum composed of m Lorentzians of intensity I_i, position δ_i and half line-width Γ_i, is given by (Müller 1980, p. 3.23)

$$F(v) = g\left(N_\infty - \sum_{i=1}^{m} \frac{I_i}{1 + X_i^2} \right) ,$$

$$\text{where} \quad X_i^2 = \frac{v - \delta_i}{\Gamma_i} . \qquad (5.1)$$

N_∞ is the base line of the spectrum. The quantity g is the geometry factor. When the moving source is in its center position where the velocity is at a maximum, the count rate is N_o. When the source is moving towards the detector the count rate is higher than N_∞ and smaller in the opposite direction, see *Fig. 5.5.1.* This is the geometric effect and is taken into account by the geometry factor g. This factor is a function of the velocity of the source and contains one adjustable parameter which is determined in the fit routine.

Equation *(5.1)* is used in the program MÖSSFUN to fit the data points. MÖSSFUN requires 1024 data points or less for analysis. Data from a raw spectrum (2048 channels) was changed to meet this requirement by adding adjacent channels. The parameters of each line, the geometric effect parameter, and the base line are varied so that a "least squares fit" of the data is obtained. The "goodness of fit" is judged from the χ^2 value calculated at the end of a fit procedure. The final output of MÖSSFUN is a list of values for the parameters of each sub-spectrum. The first half and its mirror image (the second half) are fitted simultaneously and this effectively doubles the number of lines that have to be fitted in a ME spectrum. This results in a more reliable fit to the data. Furthermore, if only one half of the spectrum is fitted, the base line which is important for calculations of the absorption areas, is distorted to obtain a "good fit". This freedom is denied to the fitting routine if both halves are fitted simultaneously.

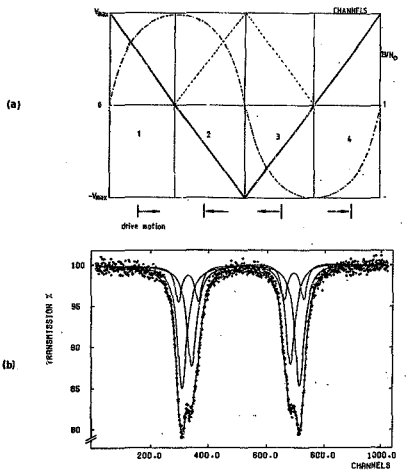


Fig. 5.5.1 (a) A calibration spectrum indicating the velocity as a function of channel (solid line). The dash-dot-dash line represents the base line B relative to the base line value N_0 obtained when the source is stationary. (b) A spectrum and its mirror image resulting from the drive motion in (a).

5.6 The Mössbauer spectra : interpretation and phase analysis.

Approximately fifteen ME spectra were measured in the temperature range 300 K to 4.6 K. The measurements above 77 K were done once each, except the room temperature measurements which were recorded both inside and outside the cryostat. Measurements below 77 K were repeated and no changes were seen to occur due to temperature cycling of the sample. *Fig. 5.6.1* is a room temperature measurement recorded with the sample in the cryostat. Three sub-spectra were used to fit the spectrum. These components correspond to Nb_3Sn, β-Sn and

$NbSn_2$. The superconducting transition temperatures of these phases are listed in *table 5.1.1*. $NbSn_2$ has a non-cubic crystal structure resulting in a quadrupole splitting. The parameters of the sub-spectra compare well with those cited in the literature (*table 5.6.1*).

In the preparation of the tape, the material is raised to a high temperature followed by a rapid cooling procedure so that the high temperature phases are retained (*fig. 5.1.1*); this accounts for the fact that no Nb_6Sn_5 component is present in our ME spectra. We are confident that the choice of components is unique as judged from the evolution of the Mössbauer spectrum as the temperature is lowered. By lowering the temperature to 77 K we do not expect any phase transformations to occur; that is, we do not expect the positions of the components to shift significantly. The shape of the spectra show drastic changes as the temperature is lowered (*fig. 5.6.2*), yet our choice of components allows us to obtain a good fit at each temperature without the need for changing the positions of the various components. The χ^2 value at room temperature was χ^2 = 1.04, where χ^2 = 1.00 represents an ideal fit, and in the worst case χ^2 = 1.42 at 175 K. This represents excellent fits to the data bearing in mind that both halves of the spectrum were fitted simultaneously (see §5.5).

The change in the shape of spectrum is due to the change in areas of the various components, which is due to the change in the recoilless fraction of Sn in the various phases as a function of temperature. The ratio of the absorption areas of sub-spectra in a Mössbauer spectrum allows the determination of the relative proportions of the various phases present. This follows from equation (*2.12*) if the f values for Sn in the various phases is known. That is, the proportion of phase 1 material (n_1) to phase 2 material (n_2) can be obtained from

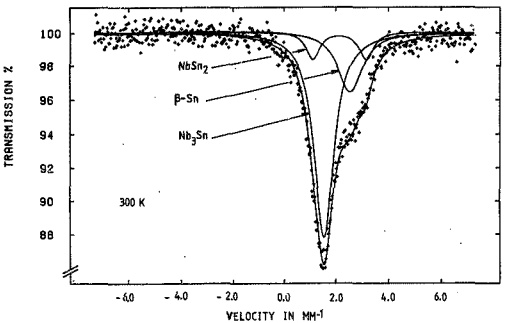


Fig. 5.6.1 Mössbauer spectrum of Nb-Sn superconducting tape at room temperature.

$$\frac{A_1}{A_2} \approx \frac{n_1 f_1}{n_2 f_2}. \qquad (5.2)$$

The areas A_i can be calculated from the parameters of the sub-spectra. For the case of Lorentzian line-shapes the area of a sub-spectrum is the product of the intensity and the line width normalized to the base line and the natural line-width. In order to find the f values the following analysis was performed. From equations (2.11) and (5.2) it follows that

$$\ln(A_1/A_2) = \ln(n_1/n_2) - k^2[\langle x_1^2\rangle_T - \langle x_2^2\rangle_T]. \qquad (5.3)$$

It is instructive to plot $\ln(A_1/A_2)$ as a function of temperature, where the subscript 1 refers to the phases Nb_3Sn or $NbSn_2$ and the subscript 2 refers to the pure Sn phase. This is shown in fig. 5.6.3 (a),(b). Observe in fig. 5.6.3

	sub-spectra				literature		
	$NbSn_2$	Nb_3Sn	β-Sn		$NbSn_2$	Nb_3Sn	β-Sn
δ	2.12 ± 0.04	1.54 ± 0.02	2.54 ± 0.10		2.18	1.55	2.56
Γ	0.68 ± 0.29	0.93 ± 0.05	1.17 ± 0.30		0.86	0.85	
Δ	2.06 ± 0.16	–	–		1.97	—	—

δ isomer shift
Δ quadrupole splitting
Γ line width

Table 5.6.1 Parameters (in mm/s) for a room temperature spectrum as obtained with MÖSSFUN in a least squares fit of the data ($\chi^2 \approx 1.04$) compared with values obtained in other measurements (Sitek et al. 1978, Mössbauer Effect Data Index -- Covering the 1970 Literature, p. 23).

(*a*) that at high temperatures, T ≥ 77 K, $ln(A_1/A_2)$ is linear in temperature T. Therefore equation (*5.3*), with the aid of the first term in equation (*2.15*) can be written as

$$ln(A_1/A_2) = ln(n_1/n_2) - \frac{6E_R}{k_B}\left[\frac{1}{\theta^2_{-2}(1)} - \frac{1}{\theta^2_{-2}(2)}\right]T. \qquad (5.4)$$

$\theta_{-2}(x)$ is a characteristic temperature of a Sn atom in phase x. The quantity $ln(n_1/n_2)$, the logarithm of the relative proportion of two phases, is a constant which shifts the plots in *fig. 5.6.3* up or down. Equation (*5.4*) indicates that the slope of the curve in *fig. 5.6.3* (*a*) is

$$slope = -\frac{6E_R}{k_B}\left[\frac{1}{\theta^2_{-2}(1)} - \frac{1}{\theta^2_{-2}(2)}\right]. \qquad (5.5)$$

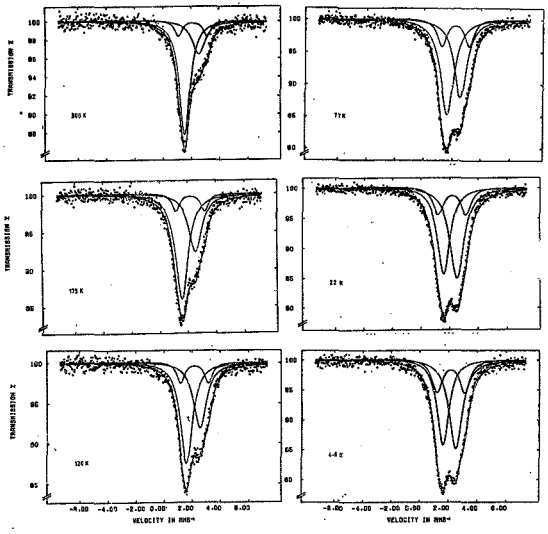


Fig. 5.6.2 Temperature evolution of the Mössbauer spectrum. Additional spectra measured at 87 K, 13 K and 9 K, are not shown.

The constant $C \equiv 6E_R/k_B$ equals 179 K. The characteristic temperature is known accurately in the case of Sn (Hohenemser 1965) and in the range 77 K $\leq T \leq$ 200 K is constant at $\theta_{-2}(\mathrm{Sn}) = 140$ K. This enables the determination $\theta^2_{-2}(\mathrm{Nb_3Sn})$ from equation (*5.5*) and *fig. 5.6.3 (a)*. A similar analysis results in the determination of $\theta^2_{-2}(\mathrm{NbSn_2})$ from *fig. 5.6.3 (b)*. The results reveal that

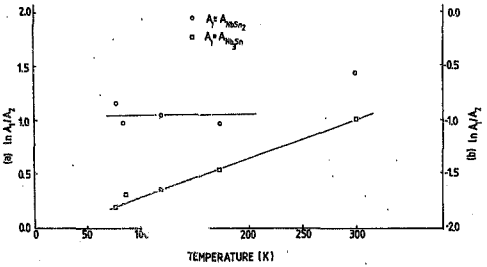


Fig. 5.6.3 A plot of $ln(A_1/A_2)$ versus temperature, where A_2 is the absorption area of the β-Sn component and A_1 is the absorption area of the Nb_3Sn component (a) ; (b) refers to the $NbSn_2$ component.

$\theta_{-2}(Nb_3Sn)$ = 176 K and $\theta_{-2}(NbSn_2)$ = 140 K. From equation (5.2) and the fact that

$$f_i = exp\ [\ -CT/\theta^2_{-2}(i)\ ], \qquad (5.6)$$

we are able to calculate the relative proportion of the phases present by using the measurements obtained at temperatures $T \geq 77$ K. The results show that the sample contains 16% $NbSn_2$, 40 % Nb_3Sn and 44 % β-Sn. These results indicate that our sample of superconducting tape has a significant proportion of the high T_C Nb_3Sn phase; this is enough to create a continuous Nb_3Sn layer rendering it useful for technological applications.

Working with the ratios of absorption areas has the added advantage of cancelling the background component. If the background is not effectively eliminated this will result in inaccurate values for the absorption areas.

5.7 Lattice Dynamics

It is appropriate to introduce some theoretical background (Kolk 1984, pp. 107-110). *Fig. 5.7.1 (a)* shows a a Lennard-Jones-type pair potential ϕ resulting from the interaction of two isolated atoms. Now consider an atom in a solid. For an atom B moving in the potential of two other atoms A and C at distances of about r_o, where r_o is the distance for which ϕ is minimal (*fig. 5.7.1 (a)*), the atomic potential ϕ_a is as shown in *fig. 5.7.1 (b)*. The mean-square displacement (msd) as a function of temperature is shown in *fig 5.7.2 (b)*. When the atomic potential is approximated by a parabolic potential (the harmonic approximation), the motions of the atoms are considered to be a superposition of 3N independent normal modes. In this case the msd of an an atom at moderate and high temperatures is given by the first order term in equation (*2.13*). The msd as a function of temperature is shown in *fig 5.7.2 (a)*. Note the difference between *fig. 5.7.2 (a)* and *fig. 5.7.2 (b)* at high temperatures. The deviation from a parabolic potential results in the anharmonic (higher order) terms in equation (*2.13*) and the corresponding high temperature anharmonic effects. For solids in which the distances between B and its neighbors exceed r_o the atomic potential is "wine-bottle like", *fig. 5.7.1 (c)*. This significant deviation from a parabolic potential results in both low temperature and high temperature deviations from harmonic behavior, and the msd as a function of temperature is shown in *fig 5.3.2 (c)*. The above indicates that the shape of ϕ_a as determined by the lattice, accounts for the temperature behavior of the msd.

We are able to plot the msd of Sn in the various phases as a function of temperature. The quantity on the left hand side of equation (*5.3*) can be evaluated from the Mössbauer spectra, the relative proportions of the phases present have been calculated in the previous section, and so the difference in the msd's of two phases can be calculated as a function of temperature. Since the msd of β-Sn as a function of temperature is known accurately from Hohenemser's meas-

urements (1965) we can find the msd's of the other two phases in the sample relative to that of β-Sn. *Fig 5.7.3* is a plot of the msd's of the other phases relative to the literature stated msd of β-Sn as a function of temperature using the areas obtained in the spectra of *fig. 5.6.2.*

The low T_C phases, β-Sn and $NbSn_2$, show similar behavior, in contrast to that of the high T_C Nb_3Sn phase. Observe that in the low temperature regime, T ≤ 77 K, the msd of Nb_3Sn is weakly temperature dependent as compared with the other two phases. The behavior of the msd of Nb_3Sn at low temperatures is consistent with the x-ray measurements of Vieland (1971) and contradicts the results of Shier and Taylor (1968) who find msd values twice as large as the x-ray measurements, implying low temperature anharmonicity, *fig. 5.7.2* (c). At high temperatures, T ≥ 200 K, the msd of β-Sn and Nb_3Sn show deviations from harmonic behavior, more so in the case of the high T_C Nb_3Sn phase. The low T_C $NbSn_2$ phase closely follows harmonic behavior. *Table 5.1.1* and *fig. 5.7.3* in-

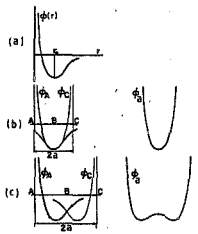


Fig. 5.7.1 *(a) Pair potential φ.* (b) The atomic potential ϕ_a when the interatomic spacing a is about r_o ; it is in reasonable approximation parabolic. *(c)* ϕ_a *deviates from* parabolic behavior when the interatomic spacing is larger than r_o.

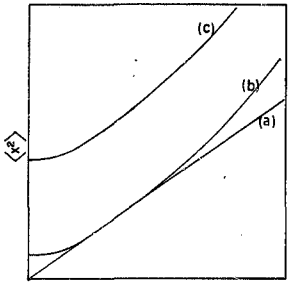


Fig. 5.7.2 The msd of an atom in the harmonic approximation (a); (b) in a potential as shown in fig. 5.7.1 (b) ; (c) in a highly anharmonic potential as shown in fig. 5.7.1 (c), according to Dash et al. (1968).

dicates that the T_c of a tin compound is related to the deviation of the tin msd from harmonic behavior -- the higher the T_c the more the degree of anharmonicity. The degree of anharmonicity is not governed by the crystal structure because *fig. 5.7.3* shows that the low T_c phases, one with a high symmetry lattice and the other with a low symmetry lattice, have similar behavior. The high T_c phase has a high symmetry lattice and shows radically different behavior.

5.8 Concluding remarks.

We have used the Mössbauer effect to determine the phase composition of a sample of Nb-Sn superconducting tape. This is important when considering the preparation procedures of superconducting materials, especially when high T_c compounds are the required end product. The results reveal that the sample contains 40 % of the high T_c Nb_3Sn phase, 16% $NbSn_2$ and 44% β-Sn.

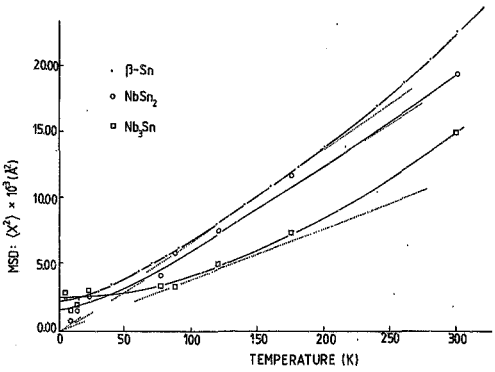


Fig. 5.7.3 The msd as a function of temperature for the various Nb-Sn phases present relative to the β-Sn measurements of Hohenemser (1965). The dotted lines represent harmonic behavior. The solid lines are drawn to guide the eye.

To aid in our understanding of what determines the superconducting transition temperature in a solid, we have examined the lattice behavior of superconducting compounds. The results indicate that there is a relation between the T_c and the lattice dynamics. It appears that the degree of anharmonicity influences the superconducting transition temperature. The high T_c phase shows a significant departure from harmonic behavior while the low T_c phases (Sn and $NbSn_2$) follow harmonic behavior closely. When one considers that anharmonic

effects are responsible for many crystal properties, indeed the ferroelectric state in certain crystals is associated with a highly anharmonic potential, it is likely that the anharmonic effects are responsible for another exotic property -- superconductivity.

The next step in the experimental programme is to obtain pure Nb-Sn phases and to perform more accurate measurements by accounting for thickness effects (Greenwood 1971, pp. 71-72), and eliminating the background component with the aid of our high resolution germanium detector. In addition to this, apparatus is being built to allow high pressure studies; the application of high pressure to a solid means changing the lattice and thus varying the degree of anharmonicity. This will provide further information about whether, and to what extent, the lattice determines the superconducting transition temperature.

ACKNOWLEDGEMENTS

I would like to acknowledge all constructive criticism and helpful suggestions offered by supervisor Prof. B. Kolk during the research programme and in the preparation of this report. Many thanks to the following people for their contributions. In the Physics department : technical staff for assistance with apparatus, and members of the academic staff for their interest in the work. Colleagues in the Mössbauer Laboratory of the Physics department for assistance and helpful discussions. V.J. Osborne for constant encouragement and almost infinite patience. Debra Nails for proof reading the report. Finally, the Council for Scientific and Industrial Research and the University of the Witwatersrand for financial support.

Bardeen J., L.N. Cooper, and J.R. Schreiffer (1957), Phys. Rev. 108, 1175.

Charlesworth J.P., Macphail I., and Madsen P.E. (1970), J. of Mater. Sci. 5, 580.

Corson M.R. (1980), Rev. Sci. Instrum. 51, 331.

Dash J.G., D.P. Johnson and W.M. Visscher (1968), Phys. Rev. 168, 1087

Glowcki B., and Chojchan J. (1983), Phys. Stat. Sol. (a) 80, K93.

Greenwood N.N. and T.C. Gibb (1971), *Mössbauer Spectroscopy*, (Chapman and Hall, London).

Hohenemser C. (1965), Phys. Rev. 139, A185.

Kimball C.W., S.P. Tanega, L. Weber and F.Y. Fradin (1974) in *Mössbauer Effect Methodology*, vol. 9, Ed. by I. J. Gruverman, C.W. Seidel and D.K. Dieterly (Plenum, New York), 93.

Kolk B. (1984) in *Dynamical Properties of Solids*, vol. 5, Ed. by G.K. Horton and A.A. Maradudin (North-Holland, Amsterdam).

Matthias B.T. (1957), Chapter 5, in *Progress in Low Temp. Physics*, Vol. 2, Ed. by C. J. Gorter (Interscience, New York).

Matthias B.T. (1976), *Superconductivity in d- and f- band metals*, (Rochester, New York).

Müller E.W. (1980), *MÖSSFUN, A New and Versatile Mössbauer Fitting Program* (distributed by the Mössbauer Effect Data Center).

Newrock R.S., D.W. Wagner and M.D. Rosenthal (1977), J. of Phys. E 10, 934.

Shier J.S., and R.D. Taylor (1968), Phys. Rev. **174**, 346.

Sitek J., J. Kruzliak, M. Tomasich, J. Cirak, and M. Presja (1978), Phys. Stat. Sol. (a) 47, K96.

Vertes A., L. Korecz and K. Burger (1979), *Mössbauer Spectroscopy*, Vol. 5 in the series *Studies in physical and theoretical chemistry*, (Elsevier, Amsterdam).

Vieland L.J. (1971), Phys. Rev. B3, 1804.

Author Hearne Giovanni Rosano
Name of thesis Mossbauer Effect Studies At Low Temperatures. 1985

PUBLISHER:
University of the Witwatersrand, Johannesburg
©2013

LEGAL NOTICES:

Copyright Notice: All materials on the University of the Witwatersrand, Johannesburg Library website are protected by South African copyright law and may not be distributed, transmitted, displayed, or otherwise published in any format, without the prior written permission of the copyright owner.

Disclaimer and Terms of Use: Provided that you maintain all copyright and other notices contained therein, you may download material (one machine readable copy and one print copy per page) for your personal and/or educational non-commercial use only.

The University of the Witwatersrand, Johannesburg, is not responsible for any errors or omissions and excludes any and all liability for any errors in or omissions from the information on the Library website.